The VN_2 negatively charged defect in diamond. A quantum mechanical investigation of the EPR response

Giulio Di Palma,[1] Bernard Kirtman,[2] Francesco Silvio Gentile,[1,*] Alexander Platonenko,[3] Anna Maria Ferrari,[1] and Roberto Dovesi[1]

[1] *Dipartimento di Chimica, Università di Torino and NIS (Nanostructured Interfaces and Surfaces) Centre, Via P. Giuria 5, 10125 Torino, Italy*

[2] *Department of Chemistry and Biochemistry, University of California, Santa Barbara, California 93106*

[3] *Institute of Solid State Physics, University of Latvia, 8 Kengaraga street, LV1063, Riga, Latvia*

(Dated: December 9, 2019)

The VN_2^- defect in diamond consists of a vacancy surrounded by two substitutional nitrogen atoms, which lower the local symmetry from T_d to C_{2v}. Calculations of the doublet ground state geometry, electronic structure, EPR parameters, and IR spectra of this defect are reported along with a preliminary investigation of the observed optical transition. For the most part our results were obtained using a uniform charge compensated supercell approach together with the B3LYP functional and *all-electron* Gaussian basis sets designed for the properties studied. In particular, the computed hyperfine and quadrupolar EPR parameters for the carbon and nitrogen atoms adjacent to the vacancy agree very well with the experiments (Fermi contact values are 245 MHz vs 241 for ^{13}C, and 4.1 vs 4.0 for ^{15}N). The accompanying spin distribution may be described as a damped spherical spin wave with little spin density on the nitrogen atoms. IR spectra show some interesting features in the range of approximately 360-1310 cm^{-1}, which are absent in the pristine diamond. Functionals without exact exchange, such as PBE, better reproduce the observed zero phonon line.

Keywords: Diamond, VN_2^- defect, VN_2^0 defect, electronic structure, band structure, IR spectrum, Electron Paramagnetic Resonance response, comparison simulation-experiment

1. INTRODUCTION

Natural and synthetic diamonds have attracted significant interest for many possible applications, such as high temperature diodes, transistors, thermistors and detectors[1,2], thanks to their high melting point, thermal conductivity, hardness and wide band gap. These properties can be dramatically modified by the presence of selected intrinsic and extrinsic defects, which can be incorporated in diamond[3–6]. Recent studies on the nitrogen vacancy defect NV, in which a substitutional nitrogen is first neighbor to a vacancy, suggest that such materials could be strong candidates for quantum technologies[7].
Nitrogen is, by far, the most common impurity and nitrogen-containing diamonds are classified as type Ib, when a single N atom is substituted for a carbon atom (N_s), or Ia when the N atoms aggregate. The most common aggregates are vicinal N_s pairs (A centers) and B defects, in which four nitrogen atoms surround a carbon vacancy (V)[8,9]. Natural diamonds are usually of type Ia, since high geological temperatures and pressures promote aggregation, while synthetic diamonds produced by chemical vapor deposition (CVD) are usually type Ib[10]. It has been demonstrated that type Ib diamonds, when subjected to HTHP (high temperature high pressure) treatments can produce significant concentrations of other aggregates, such as the VN_2^- paramagnetic defect[11] (the alternative notation N_2V^- can also be found in the literature for this defect). This center has been related to optical and paramagnetic signatures[12]. The most convincing feature regarding its identity is the H2 optical band, which was first reported in 1956 after a radiative and thermal treatment of natural diamond[13]. At 80 K the H2 band has been observed in both absorption and luminescence with a ZPL (zero phonon line) at 1.257 eV and with the appearance of a vicinal vibronic band as well[12]. Uniaxial stress and photochromism charge balance studies on the H2 ZPL show that the defect has C_{2v} symmetry[12] and is the negative charge state of the defect associated with the H3 optical band, which has been assigned to the N-V-N = VN_2^0 center[14,15]. Recent studies on ^{15}N isotopically enriched diamonds have been used to characterize the Electron Paramagnetic Resonance (EPR) spectra of the VN_2^- defect, as well as to confirm attribution of this defect to the H2 optical band[11].
In this paper we present an *ab initio* quantum chemical description of the electronic structure and microscopic ground state properties of the VN_2^- defect at the B3LYP density functional theory (DFT) level. In its ground electronic state VN_2^- is a spin doublet formed by adding an electron to the ground state of neutral VN_2^0. Of particular interest for the negatively charged defect is the electron spin distribution, which has been partially characterized experimentally[11] by analysis of the electron paramagnetic resonance (EPR) hyperfine coupling parameters. Experimental EPR hyperfine coupling parameters have been successfully computed previously for the neutral N substitutional defect (the so called C defect[16]). Here we consider, for the first time, an application of the same computational procedure to a negatively charged defect. Again, our B3LYP supercell calculations, this time obtained with uniform background charge compensation, are shown to accurately reproduce the measured values. As noted above EPR experimental data is often used,

in combination with various models, to provide a proposed microscopic characterization of a given defect - i.e. the identity, geometry, charge and spin distribution, etc. Here we proceed, instead, to solve the Schrödinger equation in order to obtain the microscopic properties including the EPR parameters. The good agreement between measured and computed EPR data, consisting of such sensitive parameters as the Fermi contact and total hyperfine coupling tensors, provides a partial validation for the microscopic description, which differs somewhat in this case from that inferred from experiment.
Although the EPR parameters and related electronic structure properties are of primary interest here, we also predict the infrared (IR) and Raman spectra (which have yet to be experimentally determined) and discuss the H2 optical band. When taken together these properties provide not only a detailed characterization of the VN_2^- defect in diamond, but by extension suggest a similar approach for other charged defects in diamond and in insulating materials in general.

In this paper the computational details are reported in Section 2. Then, in Section 3, we discuss separately: (A) the geometry of the defect along with the electronic charge and spin distributions around the vacancy site; (B) the EPR hyperfine coupling parameters; (C) the IR and Raman spectra; and (D) the orbital band structure and H2 optical transition. Finally, our conclusions and future perspectives are presented in Section 4.

2. COMPUTATIONAL METHODS

We employed the long established periodic supercell approach for treatment of the defect[19,20]. Here a supercell containing 216 atoms (215 after creation of the vacancy), and denoted in the following as S_{216}, was considered. It is a cubic cell, obtained by multiplying the conventional diamond cell (that contains 8 atoms) by 3 along the three lattice translation vectors (8x27=216). Since the unit cell of a periodic system must be neutral, for VN_2^- a uniform background positive charge density was added. Reciprocal space sampling was based on a regular Pack-Monkhorst[21] sub-lattice grid centered at the Γ point (i.e. at the center of the first Brillouin zone), leading to 4 sample points along each of the reciprocal lattice vectors. This corresponds to 24 k-points in the irreducible part of the Brillouin zone after point symmetry has been taken into account.

Our supercell electronic structure calculations utilize the global hybrid B3LYP functional[22,23] which, unlike other treatments, includes a key contribution for defects from exact exchange as implemented in the CRYSTAL program[24]. Pople's standard 6-21G[25] *all-electron* basis sets of Gaussian type functions were adopted for both carbon and nitrogen, except for the exponents of the outermost *sp* orbitals of the host and dopant atoms, increased to 0.23 and 0.30 $Bohr^{-2}$, respectively, for computational efficiency. This small basis set permits the investigation of computationally demanding properties, like the IR spectrum of large unit cell systems, as was the case of the 1000 atoms supercell of the diamond B defect[26].Polarization functions were sometimes added (i.e. 6-21G(d) basis set) for testing purposes.
A much more extended (and expensive) basis set[27] was also adopted, in particular for the calculation of the electron-nuclear spin hyperfine coupling tensor. It contains six s functions, constructed from 811111 contractions of gaussian primitives, two p type shells, constructed from 41 contractions, and a single primitive d function, for a total of 17 atomic orbitals (AOs), as compared to 9 AOs in the 6-21G basis set. It was derived from the standard 6-31G* basis set and, for this reason, is denoted 6-31G-J*. The latter was designed to better describe the core region, but also the valence shells are richer, and the most diffuse s and p gaussians are more diffuse than in the 6-21G, with exponents equal to 0.169 and 0.212 $Bohr^{-2}$ for functions on C and N, respectively.[27]. In contrast with F centers in ionic solids, ghost orbitals at the vacancy site need not be added for diamond as shown in previous calculations.
The combination of the B3LYP functional and the 6-31G-J* set has been shown to provide accurate results for the EPR parameters of the C (*i.e.* N_s) defect in diamond[16].
Truncation of the Coulomb and exchange infinite lattice series is controlled in CRYSTAL by five thresholds, T_i, that were set to 8 (T_1-T_4) and 16 (T_5). The convergence threshold on the energy for the self-consistent-field (SCF) procedure were set to 10^{-8} Hartree for structural optimizations and to 10^{-10} Hartree for vibrational frequency calculations.
The DFT exchange-correlation energy and its gradient were evaluated by numerical integration over the unit cell volume. Generation of the integration grid points is based on an atomic partition method, originally proposed by Becke[28], in which the radial and angular points are obtained from a Gauss-Legendre quadrature and a Lebedev two-dimensional distribution, respectively. The choice of a suitable grid is crucial for both numerical accuracy and cost. In this study a pruned grid with 75 radial and 974 angular points was employed.
For the band gap and the H2 optical line (see Section 3.4) we also considered finite clusters containing up to 168 carbon atoms. These calculations were done using other functionals, as well as B3LYP, together with the conventional 6-31G, 6-31G(d) and 6-311G(d) basis sets.

2.1. EPR parameters

The coupling between the spin of the unpaired electrons ($\mathbf{S}$) and the system of nuclear spins ($\mathbf{I}^n$), plus the nuclear spin-spin interactions, is described by the Hamiltonian:

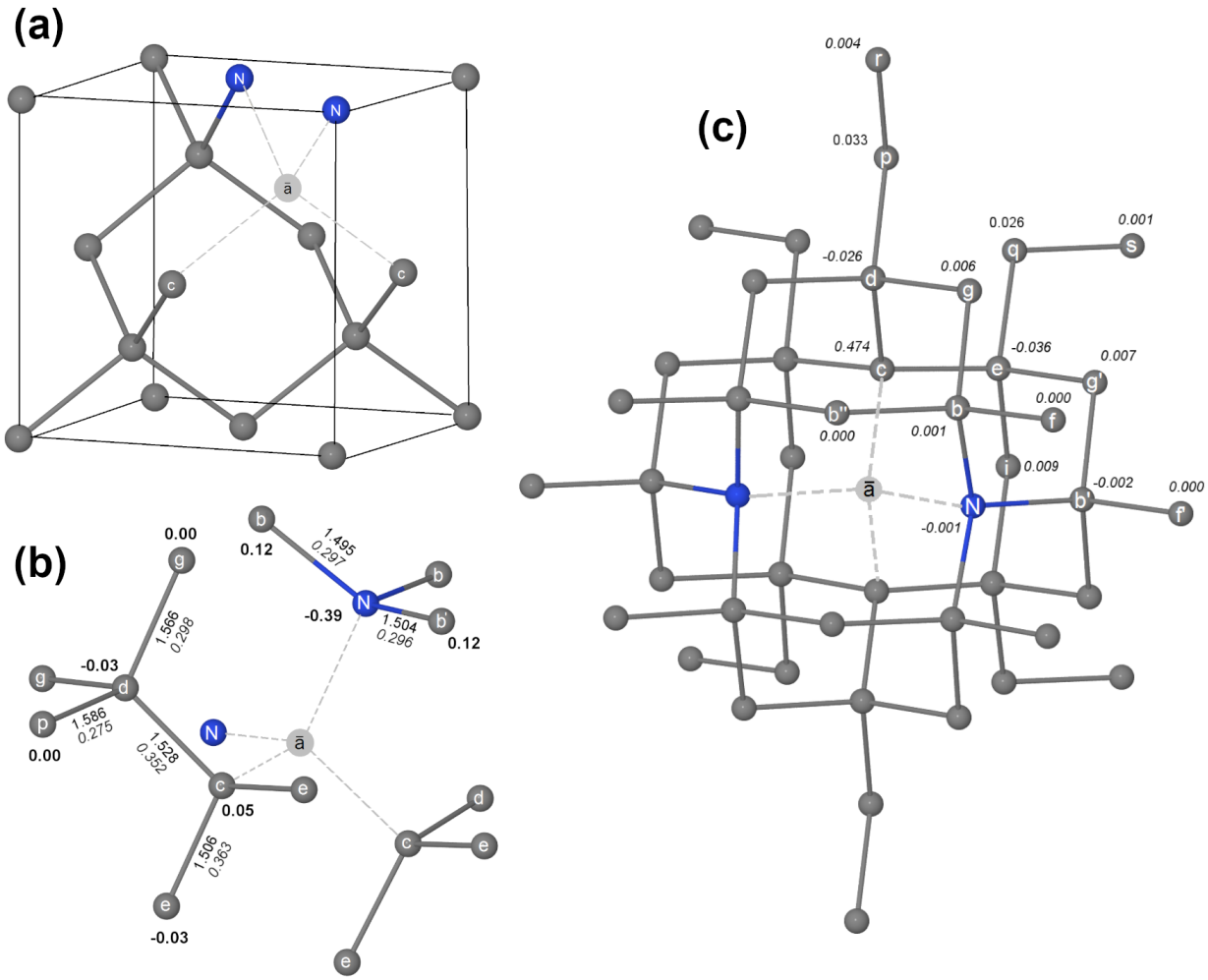

FIG. 1: The VN_2^- defect from three different perspectives (B3LYP/6-21G S_{216} supercell results): (a) the pristine diamond conventional cell; (b) the local cluster of C and N atoms adjacent to the vacancy plus 12 next-nearest neighbors; and (c) a larger cluster with all atoms having a significant spin population. The local point symmetry at the vacancy is C_{2v} and the atoms are labeled as in Refs. [17,18]. Mulliken net charges (units = |e|; boldface) are shown in (b), whereas spin populations (units = |e|; italics) are reported in (c) for each symmetry irreducible atom. Bond distances in Å and Mulliken bond populations (units = |e|; italics) are given in (b) below each pair of atoms. The population analyses were done using the B3LYP functional and 6-31G-J* basis set.

$$H = \sum_n \mathbf{S} \cdot \mathcal{A}^n \cdot \mathbf{I}^n + \sum_n \mathbf{I}^n \cdot \mathcal{P}^n \cdot \mathbf{I}^n \qquad (1)$$

Here $\mathcal{A}^n$ is the hyperfine coupling tensor for the n^{th} nucleus, at site $\mathbf{R_n}$. It can be written in the form

$$\mathcal{A}^n = A^n_{iso} \cdot \mathbb{I} + \mathcal{B}^n \qquad (2)$$

where $\mathbb{I}$ is a 3×3 identity matrix in cartesian coordinates. A^n_{iso} is the isotropic contribution to $\mathcal{A}^n$, often referred to as the *Fermi contact term*, whereas $\mathcal{B}^n$ represents the anisotropic dipole-dipole contribution. The Fermi contact term for an unpaired electron

$$A^n_{iso} = \frac{8\pi}{3} g_e \mu_e g_n \mu_N |\Psi(\mathbf{R}_n)|^2 \qquad (3)$$

arises from the direct interaction of nuclear and electron spins, and is only non-zero for states with finite electron spin density, $|\Psi(\mathbf{R}_n)|^2$, at the nuclear site $\mathbf{R}_n$. In Eq.3 the parameters g_e, μ_e, g_n and μ_N are the free-electron g-factor, Bohr magneton, gyromagnetic ratio of

$\mathbf{I}^n$ and nuclear magneton respectively. The elements of the traceless tensor $\mathcal{B}^n$ at nucleus $\mathbf{R}_n$ are defined as:

$$B^n_{ij} = g_e \mu_e g_n \mu_N \int \mathrm{d}\mathbf{r}_n |\Psi(\mathbf{r}_n)|^2 \Big(\frac{3\mathbf{r}_{ni}\mathbf{r}_{nj} - |\mathbf{r}_n|^2 \delta_{ij}}{|\mathbf{r}_n|^5} \Big) \tag{4}$$

where $\mathbf{r}_n$ is the electron distance to the nucleus at $\mathbf{R}_n$. In Eq.1, $\mathcal{P}^n$ is the quadrupole interaction tensor at the nucleus of the nth atom. This traceless tensor describes the interaction between the electric field gradient and the asymmetric charge distribution of the nucleus (for nuclear spin ≥ 1). As in the case of the $\mathcal{B}^n$ tensor (see below), one is usually interested in the diagonal components along principal axes. In fact, frequently only the largest eigenvalue is determined.
In the presence of axial symmetry the sole independent component, $P_\parallel = 3/2\ \mathrm{P}_z$ can be written as:

$$P_\parallel = \frac{3e^2qQ}{4I(2I-1)} \tag{5}$$

in which Q is the nuclear quadrupole moment, e is the electronic charge and eq= V_{zz} is the z component of the diagonal EFG (electric field gradient) tensor at the nucleus. The definition of V_{zz} is the same as that of B^n_{zz}, given in Eq.4, except that $|\Psi(\mathbf{r}_n)|^2$ is replaced by the total external charge density.
The three principal axis eigenvalues of $\mathcal{B}^n$ may be designated as B^n_1, B^n_2, and B^n_3. They measure the unpaired electron populations of valence p and d orbitals centered on the magnetic nucleus and include also the non-spherical contribution from all orbitals centered on neighboring atoms. Clearly, $A^n_{iso} = (A^n_1 + A^n_2 + A^n_3)/3$, since $\mathcal{B}^n$ is traceless. Thus, for a nuclear site with axial symmetry, $A^n_{iso} = (A^n_\parallel + 2A^n_\perp)/3$ and $B^n_\parallel + 2B^n_\perp$=0. An important point to note in electronic structure calculations, is that A^n_{iso} and B^n_{ij} reflect different aspects of the wavefunction. Whereas A^n_{iso}, as indicated in Eq.3, is determined by the electron density at the nuclear positions, B^n_{ij} samples longer range properties of the wavefunction as a result of the r^{-3} scaling in the integrand of Eq.4. It is essential, therefore, for basis sets to be sufficiently flexible so that these differing dependencies can be adequately described.
For later discussion in Section 3 we present here the electron spin data we have obtained that is relevant for calculation of the EPR parameters. Thus, the Mulliken atomic electron spin populations μ are shown in Figure 1, along with the local geometry around the defect as well as the Mulliken net atomic charges. Likewise, our spin density maps are displayed in Figure 2. These maps constitute a 2D representation of the 3D spin density function that, when integrated according to Eq.4, provides the electronic contribution to the B^n_{ij} values. When the spin densities are partitioned according to the Mulliken scheme, the μ values of Table I are obtained. The spin density along a path connecting the nuclei with large A^n_{iso} values is shown in Figure 3.

2.2. Phonon Spectra

Harmonic phonon frequencies, ω_p, at the Γ point were obtained by diagonalization of the mass-weighted Hessian matrix of second energy derivatives with respect to atomic displacements $\mathbf{u}$[29–33]:

$$W^\Gamma_{ai,bj} = \frac{H^{\mathbf{0}}_{ai,bj}}{\sqrt{M_a M_b}} \quad ; \quad H^{\mathbf{0}}_{ai,bj} = \left(\frac{\partial^2 E}{\partial u^{\mathbf{0}}_{ai} \partial u^{\mathbf{0}}_{bj}} \right) \tag{6}$$

Here atoms a and b (with atomic masses M_a and M_b) in the reference cell (indicated by superscript $\mathbf{0}$) are displaced along the ith and jth Cartesian directions, respectively. First order derivatives are computed analytically, whereas second order derivatives are obtained numerically by a two-point formula using the gradient at the equilibrium position and at a displacement of 0.003 Bohr along each cartesian coordinate (note that the gradient at equlibrium is not exactly null, but simply lower than the threshold of the optimizer). Integrated intensities for IR absorption $\mathcal{I}_p$ were determined from the Born effective charge tensor $\vec{Z}_p$[34,35] obtained using a CPHF/KS analytical method[36,37]:

$$\mathcal{I}_p \propto \left| \vec{Z}_p \right|^2 \quad ; \quad \vec{Z}_p = \frac{\partial \vec{\mu}}{\partial Q_p}. \tag{7}$$

Relative Raman intensities were computed analytically via a related scheme[38,39].

2.3. Band structure and optical lines

In the supercell calculations the band structure was obtained as described above and the energy of the ZPL (i.e. H2 line) was roughly estimated from the direct band gap at the Γ point. For the finite clusters we obtained not only the HOMO-LUMO gaps, but also obtained the energy of the H2 line from time-dependent DFT (TDDFT) calculations using the Tamm-Dancoff Approximation (TDA)[40] implemented in the ORCA code[41]. As mentioned earlier the latter calculations were done with various functionals (see Section 3.4), including B3LYP, together with the conventional 6-31G, 6-31G(d) and 6-311G(d) basis sets.

System		Q_C	Q_N	μ_C	μ_N	R_{CC}	R_{NC}	b_{CC}	b_{NC}	ΔE_{hl}
VN_2^0	s	+0.12(2)	-0.40(2)	±0.811(2)	±0.000(2)	[1.508,1.524]	[1.507,1.508]	+[0.332,0.333]	+[0.287,0.289]	+0.41
	t	+0.12(2)	-0.40(2)	+0.888(2)	+0.054(2)	[1.504,1.510]	[1.506,1.515]	+[0.335,0.338]	+[0.284,0.285]	
VN_2^-	d	+0.06(2)	-0.39(2)	+0.474(2)	-0.001(2)	[1.506,1.528]	[1.495,1.504]	+[0.352,0.363]	+[0.296,0.297]	+1.46
	q	+0.11(2)	-0.38(2)	+0.884(2)	+0.083(2)	[1.508,1.513]	[1.518,1.535]	+[0.333,0.336]	+[0.241,0.243]	

TABLE I: Atomic Mulliken spin populations μ, net charges Q and bond populations b (in |e|) for the carbon and nitrogen atoms adjacent to the vacancy in the VN_2^- and VN_2^0 defects. Values were obtained for the doublet (d) and quadruplet (q) spin states of VN_2^-, and for the triplet (t) and singlet (s) spin states of VN_2^0 through B3LYP/6-21G calculations using the S_{216} supercell. Energy differences between high and low spin states ΔE (in eV) are reported. Multiplicity is in parenthesis. Distances R (in Å) and bond populations b refer to nearest neighbors of the nitrogen and carbon atoms adjacent to the vacancy. The two different symmetry-allowed values for these properties are indicated in square brackets.

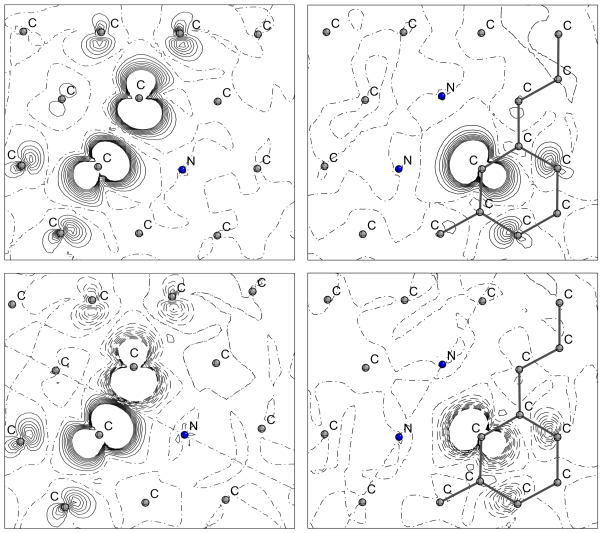

FIG. 2: Spin density map for the VN_2^- (top) and VN_2^0 (bottom) defects in their ground spin states. The two carbon atoms (gray) and one of the nitrogen atoms (blue) surrounding the vacancy define the plane of each figure on the left, while the two nitrogens and one carbon define the plane of each figure on the right. Isodensity lines differ by 0.01 |e| /(a_0^3). Spin density is truncated at ±0.1 |e| /(a_0^3). Continuous and dot-dashed lines represent positive and null spin density, respectively. All calculations were done with the S_{216} supercell, B3LYP functional and 6-31G-J* basis set.

3. RESULTS

3.1. Geometry, atomic charges and electron spin densities

The conventional cell of diamond containing the VN_2^0 or VN_2^- defect is shown in Figure 1. Removal of a carbon atom ($\bar{a}$) and the substitution of two adjacent carbons with two nitrogen atoms lowers the symmetry from T_d to C_{2v}, leaving two dangling bonds on the remaining two C atoms (C_c) around the vacancy. Each C_c, in turn, is bonded to two equivalent carbon atoms (e) and an inequivalent carbon atom (d). In the neutral VN_2^0 defect the two unpaired electrons in the dangling bonds can exist in a triplet (S_z=1) or a singlet (S_z=0) state. The triplet state is calculated to be less stable than the singlet by 0.41 eV at the spin-polarized B3LYP/6-21G level. When the defect is negatively charged, the possible spin states are a quadruplet (S_z=3/2) and a doublet (S_z=1/2). The doublet state is calculated to be 1.46 eV more stable than the quadruplet at the same level as above. Thus, in both cases the low spin state is the most stable, presumably due to Pauli repulsion between the electrons in the dangling bonds.

The local geometry of the ground state VN_2^- defect about the vacancy site is distorted from the pristine diamond structure. For the C_c-C_c distance we obtain a value of 2.624 Å compared to 2.550 Å in pristine diamond; the C_c-N distance is 2.744 Å whereas the N-N distance is 2.789 Å. With regard to the next-nearest neighbors, the $\sphericalangle$ $C_eC_cC_e$, $\sphericalangle$ $C_eC_cC_d$, $\sphericalangle$ C_bNC_b and $\sphericalangle$ $C_bNC_{b'}$ bond angles are 111.5°, 113.3°, 113.3° and 113.2° respectively compared to the smaller tetrahedral value of 109.4° for all C-C-C bond angles in pristine diamond. The nearest neighbor C-C bond lengths are reduced from those found in pristine diamond (1.545 Å) to 1.506 Å (C_c-C_e) and 1.528 Å (C_c-C_d). For nearest neighbor to next-nearest neighbor bonds the deviation changes sign and is reduced in magnitude. Beyond that, however, the bond lengths are the same as in pristine diamond within 0.01 Å. A similar behavior is seen for the C-C bond distances along the N-C profile starting with the two R_{NC} bond lengths of 1.495 and 1.504 Å, which are somewhat shorter than the corresponding nearest neighbor C_c-C_e and C_c-C_d bond distances.

It is of interest to consider the spin distribution for the VN_2^- defect in the doublet ground state where the difference in the Mulliken charge between majority and minority spins, μ_s, is +0.474 |e| on each of the two C atoms adjacent to the vacancy, and just -0.001 |e| on the N atoms. Although it seems, at first glance, that essentially the entire net spin population of +1.000 |e| is localized on the C atoms adjacent to the vacancy such is not the case. If one includes the 12 next-nearest neighbors to the vacancy site, then the sum of μ_s values is reduced from +0.95 to +0.75 |e|. Our B3LYP calculations, then, give a spin distribution that can be characterized as a damped spherical spin wave. A

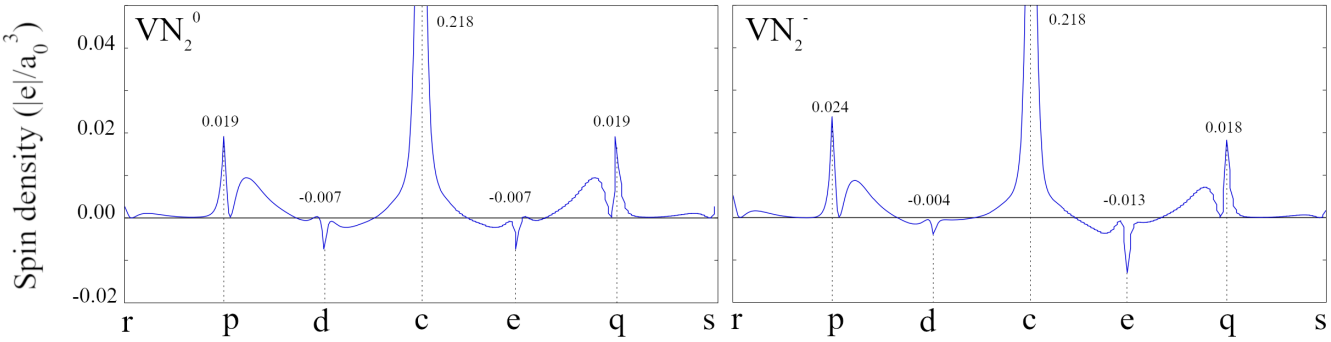

FIG. 3: Spin density profiles for the VN_2^- and VN_2^0 defects along a path connecting the atoms with relatively high spin density. Atomic labels as in panel (c) of Figure 1. All calculations were done with the S_{216} supercell, B3LYP functional and 6-31G-J* basis set.

calculation of $< S^2 >$ for the supercell gives 0.752, as compared to the theoretical value of 0.750 for a pure doublet. Hence, this behavior is not an artifact of spin contamination. The highest occupied crystalline orbital of majority spin is also strongly delocalized. Whereas this orbital has only small components on the 12 next-nearest neighbors, the next set of neighbors accounts for approximately 1/3 as much Mulliken charge as the C atoms immediately adjacent to the vacancy (the orbital coefficients on the N atoms are very small). Our prediction of the delocalized electron spin distribution contrasts with the localized picture proposed by Green, et al.[11] in connection with their interpretation of the ^{15}N anisotropic hyperfine interaction in the EPR spectrum of VN_2^-. In other respects, however, the model of Green, et al. does agree with our calculations. In either case the highest occupied orbital of majority spin is anti-bonding (b_1 symmetry) between the two carbons adjacent to the vacancy and the local orbital hybridization is very close to $s^{0.15}$ $p^{0.85}$. On the other hand, we find that the p orbital on each of these carbons points directly at the vacancy rather than at one of the nitrogens and, in addition, the separation of the C_c and N atoms is 2.74 Å as opposed to 2.1 Å in their treatment.

The 2D spin density maps and 1D spin profiles for VN_2^0 and VN_2^- are reported in Figures 2 and 3 respectively. It is interesting to observe that the magnitude of the spin densities (where relatively large) is very similar for both defects. What is different are the relative signs, which are determined by orbital symmetry. Thus, for example, in the neutral defect the net spin populations on the C atoms adjacent to the vacancy are of opposite sign and cancel in determining S_z. On the contrary, they add in the case of the charged defect.

For VN_2^- the excess negative charge, like the spin density, is strongly delocalized. The details, however, are very different. The N atoms, which have no net spin population, account together for a charge of -0.770 (out of -1.000) |e|. The C atoms adjacent to the vacancy are positively charged so that, in sum, the four nearest neighbors of the vacancy account for only 0.656 |e| of the excess electronic charge. The C atoms in the set of next-nearest neighbors that are bonded to C are negatively charged, but less so than the corresponding C atoms bonded to N. Thus, the cluster of 16 atoms is almost neutral (net charge -0.038 |e|).

3.2. Electron Paramagnetic Resonance Parameters

Recently, using diamond doped with ^{15}N isotopically enriched N_2 gas, Green *et al.*.[11] were able to obtain the EPR spectrum of the VN_2^- defect. From their spectrum they extracted the ^{15}N and ^{13}C hyperfine interaction parameters for the four atoms surrounding the vacancy. For comparison we computed the same parameters (see Table II) utilizing the S_{216} supercell, B3LYP functional and 6-31G-J* basis set, as discussed in Section 2. Our A_{iso} values are in excellent agreement with experiment being greater than the measured values by less than 3 % and 2 % for ^{15}N and ^{13}C respectively (as compared to 12 % and 19 % for 6-21G). A similar situation was found for the eigenvalues of the $\mathcal{B}^n$ tensor as can readily be seen from the table. This provides a theoretical confirmation of the assignment and, at the same time, establishes the validity of our computational procedure for the negative defect. Good agreement with experiment was also previously observed for the neutral N_s substitutional defect (C defect)[16] using similar methodology. Hence, our computational model seems able to provide results of high quality for both charged and neutral defects. In addition to the hyperfine parameters for the atoms immediately adjacent to the vacancy we report values in Table II for the C atoms further removed, which can be used to characterize the damped spin density wave. Unfortunately, no experimental data is available for comparison. Finally, electric field gradients (EFGs) were computed for every atom of the supercell. In particular, for the N atom of the

Site		A_{iso}	B_1	B_2	B_3	Ref.
^{14}N		-2.95	0.40	-0.35	-0.06	This work
^{15}N		+4.14	-0.57	+0.49	+0.08	”
		+4.02	-0.55	+0.49	+0.07	[11]
$^{13}C_1$	(c)	+245.14	+80.57	-40.48	-40.09	This work
	(c)	+240.70	+76.80	-38.40	-38.40	[11]
$^{13}C_2$	(p)	+26.77	+5.72	-2.93	-2.78	This work
$^{13}C_3$	(q)	+20.60	+4.76	-2.52	-2.24	”
$^{13}C_4$	(e)	-14.63	+1.70	-0.99	-0.71	”
$^{13}C_5$	(g’)	+7.12	+1.80	-0.94	-0.86	”
$^{13}C_6$	(r)	+5.89	+1.37	-0.74	-0.64	”
$^{13}C_7$	(d)	-4.39	+3.55	-1.96	-1.59	”
$^{13}C_8$	(g)	+4.01	+1.41	-0.86	-0.55	”
-	-	-	-	-	-	-
$^{13}C_{20}$	(b’)	-0.86	+1.03	-0.63	-0.40	This work
$^{13}C_{21}$	(b)	+0.76	+0.91	-0.65	-0.27	This work

TABLE II: Hyperfine coupling constants (MHz) for the doublet ground state of the VN_2^- defect. $\mathcal{B}$ tensor components are sorted so that $|B_1| > |B_2| > |B_3|$. The constants are sorted in descending $|A_{\rm iso}|$ order for the carbon atoms (from C_1 to C_8). C_{20} and C_{21} are the two types of carbon atoms directly linked to one of the two equivalent nitrogen atoms of the defect. The atom labels (in parentheses) are those shown in Figure 1. All values obtained for the S_{216} supercell, with the B3LYP functional and the 6-31G-J* basis set.

defect the calculated $P_{||}$ value is -5.52 MHz, while that measured by Green et al.[11] is approximately -5.0 MHz.

3.3. IR and Raman Spectra

Pristine diamond has a very simple vibrational spectrum. There is a single peak at 1332 cm^{-1} that appears in the Raman[42] and no features in the infrared (IR). In principle, then, this opens the possibility of characterizing defects in diamond through their vibrational spectra. As a check on the accuracy of our calculations we obtained the B3LYP/6-21G Raman active harmonic frequency of perfect diamond at 1317 cm^{-1}, which is in good agreement with the measured value[43] of 1332 cm^{-1}. Unfortunately, neither the VN_2^0 nor the VN_2^- defect is predicted to show any significant difference in their Raman spectra from pristine diamond, which was also found to be the case for the A, B and C defects previously studied[16,44,45]. We, therefore, focused our attention on the simulated IR spectra, based on the harmonic approximation, which are reported in the right hand column of Figure 4.
The peaks in the IR spectrum of VN_2^- span the range from 360 to 1310 cm^{-1} with the highest intensity around 1192 cm^{-1}. In comparing with the VN_2^0 defect we see that the negative charge leads to an overall increase in intensity, a shift of the highest frequency vibrations to higher frequency, and significant differences in the low frequency region. In particular, the isolated mode at 116 cm^{-1}, that appears for the neutral defect, is absent from the IR spectrum of the charged defect. It corresponds to a local scissors motion of the two C atoms adjacent to the vacancy. Graphical animations of the vibrational normal modes for each defect have been generated and confirm this interpretation[46].
In order to assess the effect of possible interaction between defects on the IR spectrum we carried out calculations using a smaller 64 atom supercell (S_{64}). Our results are shown in the left hand column of Figure 4. They indicate that such interactions can have a significant effect on the line positions and relative intensities depending, of course, on the impurity concentration.

3.4. Preliminary Study of Orbital Band Gap and H2 Optical Line

Although the EPR parameters are the primary concern of this paper we do obtain band structures as a by-product and they, in turn, have led us to a very preliminary consideration of the H2 (zero phonon) optical line. Band structures for the neutral and negatively charged VN_2 defects are shown in Figure 5 for the two different size supecells. Note that the defect levels that occur in the band gap of the diamond host exhibit a slight energy dispersion in the smaller supercell but are essentially flat in S_{216}. In the discussion below the numerical values presented refer to the larger supercell.
For the negative defect the B3LYP/6-21G direct band gap at the Γ point turns out to be 2.53 eV (see Figure 5). This is the gap associated with minority spin (shown in red), which is the smaller of the two spin values. Larger basis sets containing polarization functions (6-21G(d) and 6-311G(d) were found to have a negligible effect on the calculated gap, which is substantially larger than the transition energy of 1.26 eV observed for the H2 optical line[12].
Such a large difference could arise for a number of different reasons. But, first, we considered whether it might be due, at least in part, to our uniform charge compensation treatment. For that purpose we carried out calculations of the HOMO-LUMO gap for finite clusters, which do not require uniform charge compensation. Two different clusters were constructed by cutting the periodic crystal structure and saturating the dangling bonds at the surface with hydrogen atoms. The smaller one ($C_{68}H_{60}N_2$) contained 5 atom stars of neighbors and is designated in the following as C_{68}, while the larger one contained 6 atom stars ($C_{162}H_{100}N_2$) and is designated as C_{162}. The corresponding HOMO-LUMO gaps, 2.74 eV for C_{68} and 2.52 eV for C_{162}, showed good convergence with cluster size and good agreement with the periodic system value of 2.53 eV.
Given that the uniform charge compensation treat-

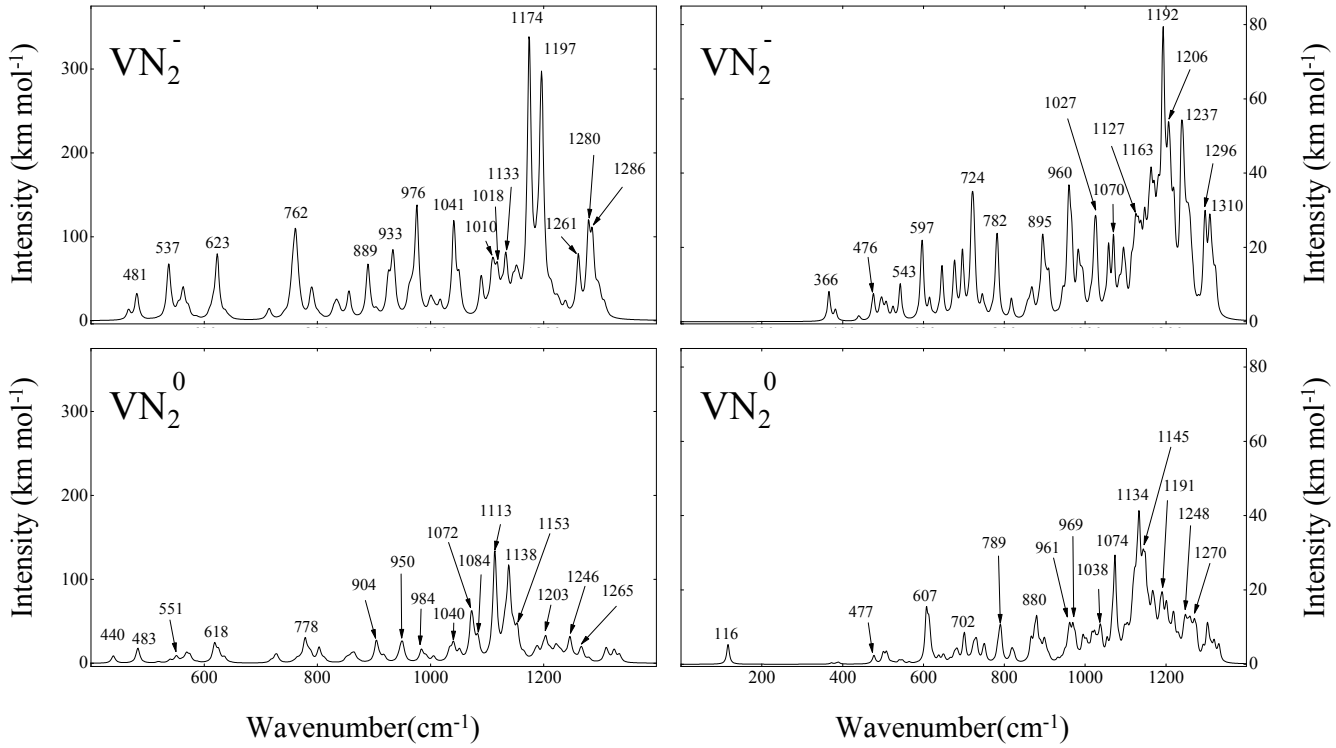

FIG. 4: IR spectra of the VN_2^- (top panels) and VN_2^0 defects (bottom panels). Data refer to two different defect concentrations, as determined by the S_{64} (left) and S_{216} (right) supercells. A Lorentzian of 8 cm^{-1} FWHM has been used for the convolution of the spectra. All calculations were done with the B3LYP functional and 6-21G basis set.

ment appears to be satisfactory we turned to time-dependent DFT (TDDFT) to test the role of configuration mixing using the Tamm-Dancoff approximation (TDDFT/TDA)[40] as implemented in the ORCA program[41]. Even though the lowest transition is dominated by the HOMO→LUMO excitation it turns out that configuration mixing has a substantial lowering effect. For C_{68} and C_{162} the predicted excitation energies in the 6-31G(d) basis are 2.03 eV and 1.90 eV, respectively. A natural transition orbital analysis reveals that the transition hole/particle pair is strongly localized on the two carbons adjacent to the vacancy. Clearly, the TDDFT/TDA calculations exhibit good convergence with cluster size and closer agreement with experiment. However, there remains a sizable discrepancy. B3LYP usually gives more similar values, but there is little experience for large anions. With that in mind we reconsidered the infinite periodic system using other functionals. Our results, then, fell into two categories - either the functional contained exact exchange or it did not. In the former case the band gap was always close to the B3LYP value; in the latter case the result was 1.33 +/- .01 eV (for the Local Density Approximation, LDA[47,48], and for two functionals belonging to the family of the Gradient Corrected Approximations (GGA), PBE[49], and PBEsol[50], the latter being a reparametrized version of the former for solids) in good agreement with the H2 optical line.

Clearly, the preliminary results described above are worthy of further investigation. For example, we did not undertake TDDFT/TDA calculations using the PBE or PBEsol functionals, although there is reason to believe that the effect of configuration mixing will be fairly small. Nor did we proceed with VN_2^0, which would be important for comparison purposes. On the other hand, since the primary purpose of the current paper is to characterize and compute EPR parameters for the negative defect, it was decided not to go beyond this preliminary study of the band gap and H2 optical line.

4. CONCLUSIONS

The structural, electronic, EPR hyperfine and vibrational characterization of the negative VN_2^- defect in diamond has been performed by means of periodic supercell quantum mechanical simulations and compared, where appropriate, with the neutral VN_2^0 defect. Uniform charge compensated supercells containing 216 atoms were employed along with the B3LYP functional and basis sets designed for the properties studied.

According to our first principles calculations the ground state of VN_2^- is a spin doublet, whereas VN_2^0 is a singlet. In either case we observe a local shortening of the distances between the carbon atoms surrounding the C_{2v}

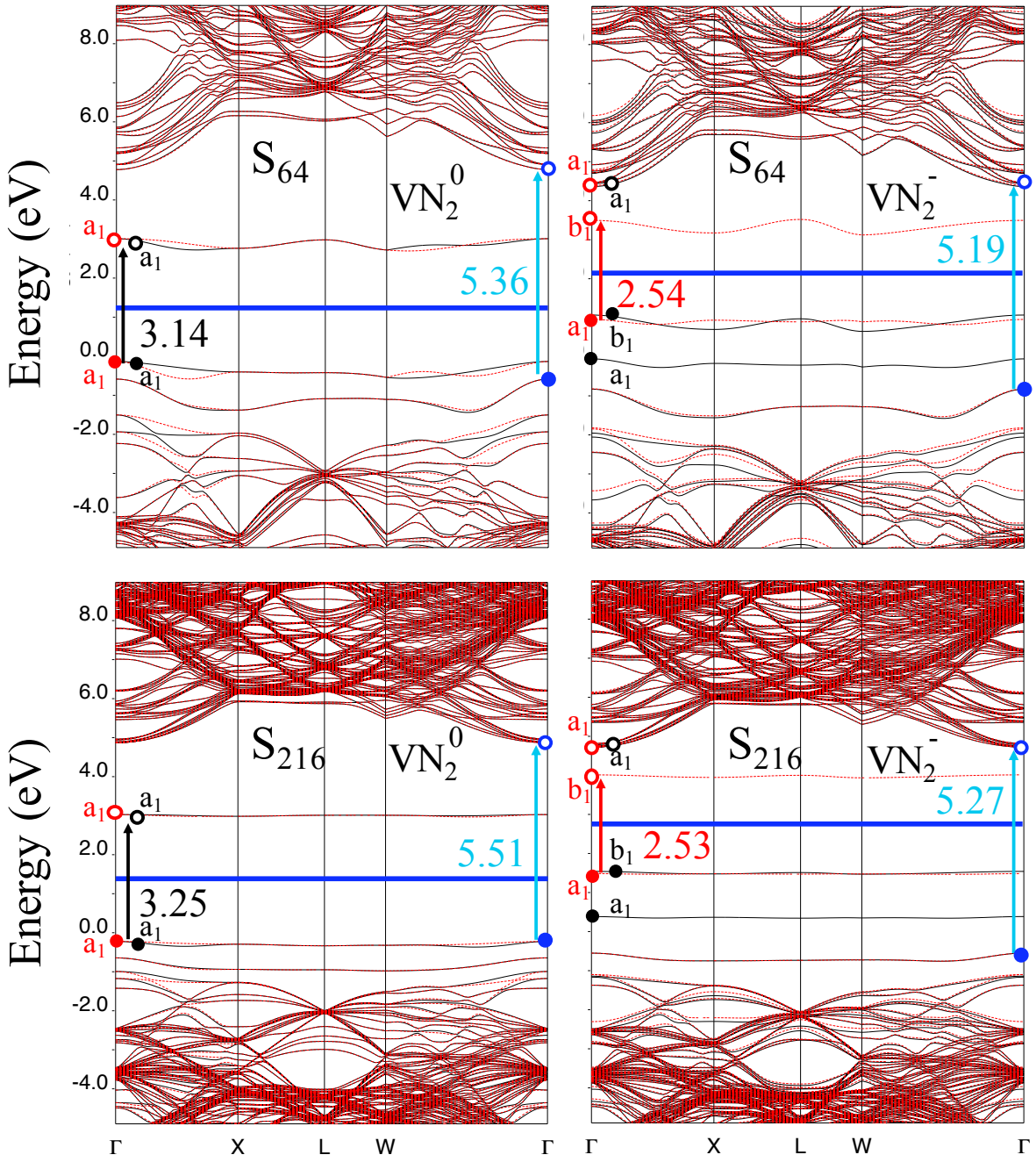

FIG. 5: Band structures for the VN_2^- (right) and VN_2^0 (left) defects obtained using B3LYP with the 6-21G basis set. Black and red lines are used to represent the majority and minority spin levels, respectively. Filled circles mark the valence bands introduced by the defect while empty circles indicate the defect conduction bands, as determined by examining the orbital coefficients. Filled and empty blue circles, together with turquoise vertical arrows, indicate the gap in the host. A symmetry label has been assigned the bands around the Fermi levels, which are represented by horizontal blue lines.

vacant site and their first and second-nearest neighbors. The calculated hyperfine and quadrupolar EPR parameters for C and N adjacent to the vacancy agree very well with experimental data. Our analysis of the wavefunction leads to a delocalized model of the spin (and charge) density around the defect site, contrasting with the localized picture previously proposed for the VN_2^- defect by Green, et al.[11]. Atomic spin densities for both defects are very similar in magnitude. In agreement with Green, et al. the highest occupied majority spin orbital of VN_2^- is anti-bonding between the two carbon atoms surrounding the vacancy and the local orbital hybridization is approximately $s^{0.15}$ $p^{0.85}$.

IR spectra of the two defects show significant differences

although the main features for both lie in the range between 360 and 1310 cm^{-1}. For VN_2^0 we observe an additional peak at 116 cm^{-1}, which is a local scissoring mode between the two carbon atoms with opposite spin surrounding the vacancy.
The B3LYP direct band gap of the VN_2^- defect at the Gamma point is much larger than the experimental transition energy for the zero phonon optical line. Preliminary TDDFT/TDA finite cluster calculations of the transition energy, reduce this difference somewhat. On the other hand, functionals without exact exchange (e.g. PBE and PBEsol) bring the calculations into agreement with observation.
The present investigation shows that the combined use of various techniques (EPR, IR, Raman, optical excitations), available at low cost in modern computer codes, could be applied to the identification of a broad class of defects in insulating materials. This is particularly true when, due to heavy irradiation, very high defect concentrations reduce the effectiveness of the optical methods.

* Electronic address: francesco.gentile@unina.it

[1] J. Bade, S. Sahaida, B. Stoner, J. Von Windheim, J. Glass, K. Miyata, K. Nishimura, and K. Kobashi, Diam. Relat. Mater. **2**, 816 (1993).
[2] P. Bergonzo, D. Tromson, and C. Mer, J. Synchrotron Radiat. **13**, 151 (2006).
[3] G. Davies, J. Phys. C **9**, L537 (1976).
[4] G. Davies, B. Campbell, A. Mainwood, M. Newton, M. Watkins, H. Kanda, and T. Anthony, Phys. Status Solidi A **186**, 187 (2001).
[5] S. Breuer and P. Briddon, Phys. Rev. B **51**, 6984 (1995).
[6] R. Kalish, A. Reznik, S. Prawer, D. Saada, and J. Adler, Phys. Status Solidi A **174**, 83 (1999).
[7] L. Childress and R. Hanson, MRS Bull. **38**, 134 (2013).
[8] T. Evans, Z. Qi, and J. Maguire, J. Phys. C: Solid State Phys. **14**, L379 (1981).
[9] D. Zedgenizov, A. Kalinin, V. Kalinina, Y. Palyanov, and V. Shatsky, in *Doklady Earth Sciences* (Springer, 2016), vol. 466, pp. 32–37.
[10] S. Lawson, D. Fisher, D. Hunt, and M. Newton, J. Phys. Condens. Matter **10**, 6171 (1998).
[11] B. Green, M. Dale, M. Newton, and D. Fisher, Phys. Rev. B **92**, 165204 (2015).
[12] S. Lawson, G. Davies, A. Collins, and A. Mainwood, J. Phys. Condens. Matter **4**, 3439 (1992).
[13] C. Clark, R. Ditchburn, and H. Dyer, Proc. R. Soc. Lond. A **237**, 75 (1956).
[14] Y. Mita, Y. Nisida, K. Suito, A. Onodera, and S. Yazu, J. Phys. Condens. Matter **2**, 8567 (1990).
[15] G. Davies, Nature **269**, 498 (1977).
[16] A. Ferrari, S. Salustro, F. Gentile, W. Mackrodt, and R. Dovesi, Carbon **134**, 354 (2018).
[17] Smith, W.V. and Sorokin, P.P. and Gelles, I.L. and Lasher, G.J., Phys. Rev. **115**, 1546 (1959).
[18] R. Cook and D. Whiffen, Proc. R. Soc. Lond. A **295**, 99 (1966).
[19] S. Salustro, A. Ferrari, R. Orlando, and R. Dovesi, Theor. Chem. Acc. **136**, 42 (2017).
[20] F. Gentile, S. Salustro, G. Di Palma, M. Causá, P. DArco, and R. Dovesi, Theor. Chem. Acc. **137**, 154 (2018).
[21] H. Monkhorst and J. Pack, Phys. Rev. B **13**, 5188 (1976).
[22] A. D. Becke, J. Chem. Phys. **98**, 5648 (1993).
[23] C. Lee, W. Yang, and R. Parr, Phys. Rev. B **37**, 785 (1988).
[24] R. Dovesi, A. Erba, R. Orlando, C. Zicovich-Wilson, B. Civalleri, L. Maschio, M. Rérat, S. Casassa, J. Baima, S. Salustro, et al., Wiley Interdiscip. Rev. Comput. Mol. Sci **8**, e1360 (2018).
[25] J. Binkley, J. Pople, and W. Hehre, J. Am. Chem. Soc. **102**, 939 (1980).
[26] S. Salustro, A. Ferrari, F. Gentile, J. Desmarais, M. Rérat, and R. Dovesi, J. Phys. Chem. **122**, 594 (2018).
[27] H. Kjær and S. Sauer, J. Chem. Theory Comput. **7**, 4070 (2011).
[28] A. Becke, J. Chem. Phys. **88**, 2547 (1988).
[29] F. Pascale, C. Zicovich-Wilson, F. L. Gejo, B. Civalleri, R. Orlando, and R. Dovesi, J. Comput. Chem. **25**, 888 (2004).
[30] C. Zicovich-Wilson, F. Pascale, C. Roetti, V. Saunders, R. Orlando, and R. Dovesi, J. Comput. Chem. **25**, 1873 (2004).
[31] A. Erba, M. Ferrabone, R. Orlando, and R. Dovesi, J. Comput. Chem. **34**, 346 (2013).
[32] C. Carteret, M. De La Pierre, M. Dossot, F. Pascale, A. Erba, and R. Dovesi, J. Chem. Phys. **138**, 014201 (2013).
[33] J. Baima, M. Ferrabone, R. Orlando, A. Erba, and R. Dovesi, Phys. Chem. Minerals **43**, 137 (2016).
[34] G. Barrow, *Introduction to Molecular Spectroscopy* (McGraw-Hill, New York, 1962).
[35] B. Hess, L. Schaad, P. Carsky, and R. Zahradnik, Chem. Rev. **86**, 709 (1986).
[36] L. Maschio, B. Kirtman, R. Orlando, and M. Rérat, J. Chem. Phys. **137**, 204113 (pages 11) (2012).
[37] L. Maschio, B. Kirtman, M. Rérat, R. Orlando, and R. Dovesi, J. Chem. Phys. **139**, 167101 (2013).
[38] L. Maschio, B. Kirtman, M. Rérat, R. Orlando, and R. Dovesi, J. Chem. Phys. **139**, 164101 (2013).
[39] L. Maschio, B. Kirtman, M. Rérat, R. Orlando, and R. Dovesi, J. Chem. Phys. **139**, 164102 (2013).
[40] S. Hirata and M. Head-Gordon, Chem. Phys. Lett. **314**, 291 (1999).
[41] F. Neese, Wiley Interdiscip. Rev. Comput. Mol. Sci **8**, e1327 (2018).
[42] A. Zaitsev, *Optical Properties of Diamond - A Data Handbook* (Springer-Verlag, 2001).
[43] S. Solin and A. Ramdas, Phys. Rev. B **1**, 1687 (1970).
[44] S. Salustro, G. Sansone, C. Zicovich-Wilson, Y. Noel, L. Maschio, and R. Dovesi, Phys. Chem. Chem. Phys. **19**, 14478 (2017).
[45] S. Salustro, A. Ferrari, F. Gentile, J. Desmarais, M. Rérat, and R. Dovesi, J. Phys. Chem. A **122**, 594 (2018).
[46] *Animations of the Vibrational Normal Modes can be Found at the Following Link:*, http://www.crystal.unito.it/animations-of-vibrational-modes.php.
[47] P. Dirac, Proc. R. Soc. A **126**, 360 (1930).
[48] S. Vosko, L. Wilk, and M. Nusair, Can. J. of Phys. **58**, 1200 (1980).

[49] J. P. Perdew, K. Burke, and M. Ernzerhof, Phys. Rev. Lett. **77**, 3865 (1996).
[50] J. Perdew, A. Ruzsinszky, G. Csonka, O. Vydrov, G. Scuseria, L. Constantin, X. Zhou, and K. Burke, Phys. Rev. Lett. **100**, 136406 (2008).